NANO LETTERS

pubs.acs.org/NanoLett Letter

Selective CO_2 Reduction Electrocatalysis Using AgCu Nanoalloys Prepared by a "Host–Guest" Method

Marta Śliwa, Hao Zhang, Jiaxin Gao, Benjamin O. Stephens, Andrew J. Patera, David Raciti, Paul D. Hanrahan, Zoey A. Warecki, Daniel L. Foley, Kenneth JT Livi, Todd H. Brintlinger, Mitra L. Taheri, Anthony Shoji Hall,* and Thomas J. Kempa*

Cite This: *Nano Lett.* 2024, 24, 13911–13918 Read Online

ACCESS | Metrics & More | Article Recommendations | Supporting Information

ABSTRACT: Multimetallic nanoalloy catalysts have attracted considerable interest for enhancing the efficiency and selectivity of many electrochemically driven chemical processes. However, the preparation of homogeneous bimetallic alloy nanoparticles remains a challenge. Here, we present a room-temperature and scalable, host–guest approach for synthesis of dilute Cu in Ag alloy nanoparticles. In this approach, an ionic silver bromide precursor harboring exogenous Cu cations is reduced to yield ∼20 nm diameter AgCu alloy nanoparticles wherein the % Cu loading can be tuned precisely. AgCu nanoparticles with a 5% nominal loading of Cu exhibit peak activity (−0.23 mA/cm^2 normalized partial current density) and selectivity (83.2% faradaic efficiency) for CO product formation from electrocatalytic reduction of CO_2 at mild overpotentials. These AgCu nanoalloys exhibit a higher mass activity compared to Ag- and Cu-containing nanomaterials used for similar electrocatalytic transformations. Our host–guest synthesis platform holds promise for production of other nanoalloys with relevance in electrocatalysis and optics.

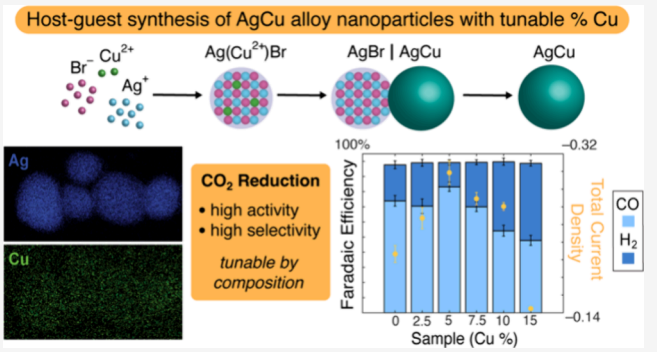

KEYWORDS: *host–guest synthesis, nanoparticles, alloys, electrocatalysis, CO_2 reduction reaction, faradaic efficiency*

Synthetic tuning of nanoparticle (NP) size, shape, and composition is central to the effective use of such materials in optoelectronic,[1−4] medical,[5−8] and energy applications. Out of the broad family of NP architectures reported to date, multicomponent NPs,[9−12] such as bimetallic and alloy NPs, have attracted interest because their properties can be engineered to reflect a hybridization or synergistic interaction between their component elements.[13] Such synergies are especially sought after in electrocatalytic applications, where the mixing of component materials can give rise to reactive sites that catalyze new reaction pathways. In bimetallic NPs, improvements to the efficiency and selectivity of electrocatalytic processes can be realized through precise control over catalytic site ensembles,[14] electronic structure tunability,[15,16] and increased stability.[14] Examples include methanol oxidation reaction catalysis with Pt–Ru catalysts,[15] ethanol oxidation over Pt–Pd NPs,[16] CO oxidation using Au–Ag alloy NPs,[17] and oxygen reduction performed over Au–Pt catalysts,[18] among many others.

The catalytic performance of alloy nanoparticles is highly sensitive to their composition, and therefore synthetic methods capable of finely regulating the concentration of any given element within the NP alloy are of paramount importance. Existing strategies for the preparation of nanoscale alloys include coreduction methods,[19] seed-mediated or two-step growth,[20] galvanic replacement,[21] the use of ionic-liquid systems,[22] or thermal decomposition techniques.[23] Many fundamental parameters, including precursor redox potential, nanoparticle lattice structure, atomic radii and melting points,[24] dictate whether the aforementioned approaches can successfully yield a desired alloy phase. It is often that an interplay of these parameters simply results in phase segregation of the component elements (e.g., if miscibility limits are exceeded), thereby limiting the applicability of these approaches. Other approaches, such as "one pot" laser ablation[25] and electrodeposition[26] techniques, use higher energies to force thermodynamic alloy products, and are limited in their ability to yield morphologically well-defined, uniform nanostructures with high product yields.

Received: June 4, 2024
Revised: October 14, 2024
Accepted: October 15, 2024
Published: October 23, 2024

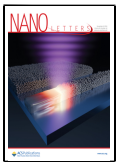

The electrochemical reduction of carbon dioxide has received extensive attention as it could be used to convert the potent greenhouse gas into feedstock chemicals. Within this context, Cu NPs have been identified as promising catalysts for the CO_2 reduction reaction (CO_2RR) primarily due to the optimal binding of the *CO intermediate[27,28] on the Cu NP surface, which in turn affords increased selectivity for C_2 and C_n reaction products. However, some limitations must be overcome. First, the catalytic activity of Cu nanoparticles is hindered by their high susceptibility to oxidation upon exposure to air.[29,30] Second, although binary phase diagrams indicate that Cu and Ag are immiscible,[31] they share a common crystal structure (fcc), accessible valence state (+1), and an approximate 15% difference in atomic radii, thereby satisfying three of four Hume−Rothery rules for metallic alloy formation.[32,33] Given these criteria, preparing bimetallic NPs with Cu as the dilute species in Ag appears to be a realistic target. Third, while a diverse array of Ag- and Cu-containing materials have been realized, the high-temperature reductions, multistep seeded growth routes, or electrodeposition approaches commonly used to prepare bimetallic Ag−Cu foams,[34] aerogels,[35] and nanoparticles[36−38] often yield materials with phase segregated components or are not well suited for industrial scale-up. Techniques do exist for forming more precise and homogeneous Ag−Cu alloy NPs, but many use dense solvents and bulky ligand-based polyol methods,[39] less convenient air-free thermal decomposition techniques,[40] or nonequilibrium rapid thermal shock treatments.[41]

In light of the need for catalytically active Ag−Cu alloys, we present here a new "host−guest" synthesis route for the preparation of phase-pure "Cu in Ag" alloy nanoparticles (AgCu NPs) and explore their performance in the electrocatalytic reduction of CO_2. We adapted our previously reported synthesis protocols[42] to prepare AgCu alloy nanoparticles with 0%, 2.5%, 5%, 7.5%, 10% and 15% nominal Cu loadings. As shown in Figure 1a, the first step (I) is formation of a silver−copper-bromide Ag(Cu^{x+})Br nanoparticle—hereafter the *host* particle. Copper cations are introduced during the synthesis of the AgBr host particle. During the next stage (II) interstitial silver and copper cation *guests* harbored in the silver halide *host* lattice are coreduced via mild solution-phase processes (Supporting Information, Materials and Methods) that lead to the precipitation of a single metallic phase on the parent Ag(Cu^{x+})Br particle surface to form AgCu|AgBr dimers. Finally, the AgBr phase is selectively digested to yield the target AgCu NPs (III).

To characterize the size and morphology of AgCu alloy NPs (Figure S1) prepared through our host−guest chemical synthesis, we used bright-field transmission electron microscopy (TEM) to image samples with 0−15% nominal Cu loadings. Analyses of TEM data collected on a 5% Cu sample reveal spherical nanoparticles with a narrow size distribution and an average diameter of 21 nm ±3 nm (Figure 1b). We also investigated particle morphology at three key stages of the synthesis. First, the average sizes of the Ag(Cu^{x+})Br host particles are comparable and unchanged across the 0−15% Cu range with mean diameters of 18−20 ± 2 nm (Figure S2). Second, following solution-phase reduction, the AgCu phases of dimer particles prepared from host particles with Cu loadings of 0, 2.5, 5 7.5, 10, and 15% Cu exhibit average diameters of 20 ± 3.5 nm, 17 ± 2.5 nm, 17 ± 3 nm, 16 ± 2.5 nm, 16 ± 2.7 and 16 ± 2.7 nm, respectively (Figure S3). Third, after etching of the dimers, the liberated AgCu NPs prepared

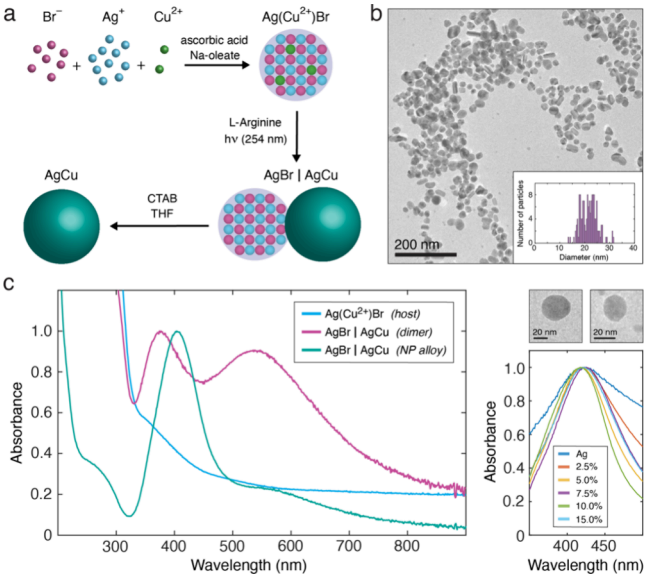

Figure 1. (a) Scheme describing key steps of the solution phase synthesis of AgCu NPs. (b) Bright-field TEM image of AgCu NPs with 5% Cu loading; Inset: Histogram of NP size. (c) Left: Absorption spectra of AgBr nanoparticles (blue trace, normalized to peak maximum at 374 nm), AgCu|AgBr dimers (purple trace, normalized to maximum at 374 nm), and 5% AgCu NPs (teal trace, normalized to maximum at 405 nm). Right: Normalized absorption spectra of AgCu NPs containing the indicated % Cu loadings focusing on the peak centered at ~408 nm. TEM images from left to right are of individual AgCu NPs with 0% and 5% Cu loadings, respectively. The features at 370 and 550 nm (dimer) may be distinct plasmon resonances associated with anisotropy in the dielectric environment around the AgCu phase: part of the AgCu is covered by ligands and solvent molecules while the remainder forms a heterointerface with the AgBr host particle.

from host particles loaded with 0, 2.5, 7.5, 10, and 15% Cu reveal average diameters of 33 ± 5 nm, 27 ± 5 nm, 21 ± 3 nm, 19 ± 4 nm, and 16 ± 2 nm, respectively (Figure S4). The AgCu NPs post etch (Figure S4) are larger than their AgCu phase counterpart in the dimer (Figure S3) likely due to continued growth and ripening of the NPs during the 12 h solution etching process.

UV−visible absorption spectroscopy was used to probe the optical properties of products generated at all key stages of the synthesis. Irradiation of the Ag(Cu^{x+})Br host particles with UV light in the presence of *L*-Arginine yields a purple solution whose absorption spectrum features peaks centered at 370 and 550 nm (Figure 1c). These peaks are not present in a solution containing the host particles before irradiation and are similar to those that we have previously ascribed[42] to dimers comprised of Ag NPs fused to their AgBr host phase. The narrow feature at 370 nm and the broad feature centered at roughly 550 nm may stem from two distinct plasmon resonances arising from the anisotropy in dielectric environment around the AgCu particle. Subsequent etching of the AgBr component of the dimer yields a yellow solution whose absorption spectrum is characterized by a single peak centered at 405 nm. This peak falls within the characteristic surface plasmon resonance band for Ag nanoparticles (λ = 360−410 nm),[43,44] and is in keeping with the expected nominal shift[45−47] of the Ag plasmon resonance with Cu doping. The two peaks characteristic of the dimer and the one peak diagnostic of the AgCu NP show no significant variation over

https://doi.org/10.1021/acs.nanolett.4c02638
Nano Lett. 2024, 24, 13911−13918

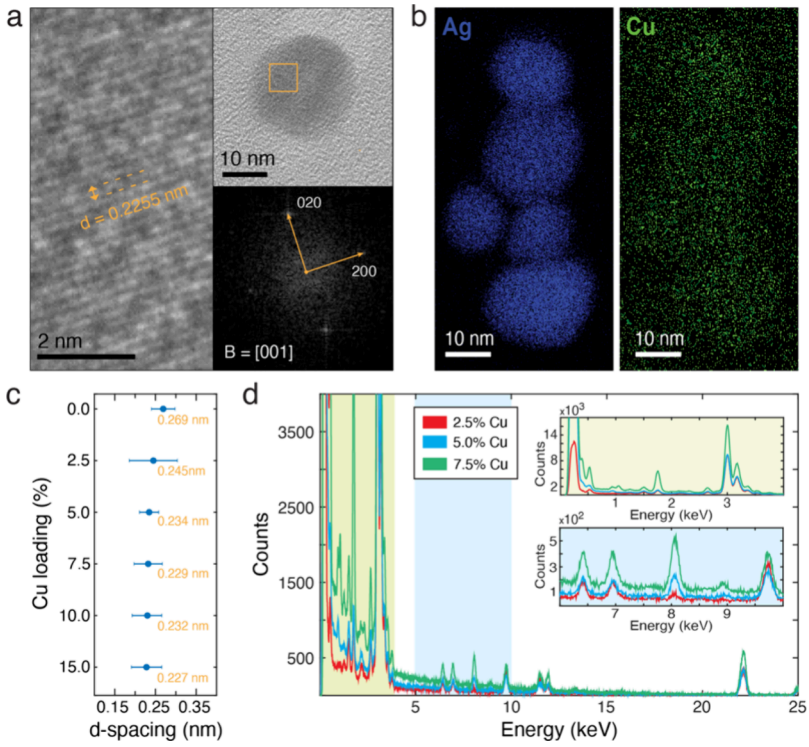

Figure 2. (a) Bright-field TEM image of a AgCu NP with 5% Cu loading and corresponding lattice image taken at high magnification. Inset: Indexed FFT-derived diffractogram acquired from the region outlined by the orange square in the TEM image above. (b) EDS maps of Ag and Cu content in a cluster of 5% Cu AgCu NPs. (c) Average *d*-spacing values (exact values in orange) for AgCu NPs across the Cu loading range. Bars denote one standard deviation. (d) EDS spectra of AgCu NPs with 2.5% (red trace), 5% (blue trace) and 7.5% (green trace) Cu loading. Light green inset reveals spectra within the 0−4 keV region that contain the Ag Lα peak (2.984 keV) and Cu Lα peak (0.93 keV). Light blue inset reveals spectra within the 6−10 keV region that contain the Cu Kα peak (8.04 keV) and the Cu Kβ peak (8.91 keV).

the range of six copper compositions (Figure 1c inset; Figure S5−S6). Likewise, all absorption peaks are well preserved upon a 10-fold increase in reagent volume (Figure S7), thus indicating the scalability of our synthetic approach. The foregoing analyses reveal that the nanoparticle alloys retain clear plasmonic signatures and suggest their promise in photocatalytic applications.

A detailed assessment of the structure and composition of the AgCu alloy NPs was carried out. Fast-Fourier transform (FFT)-derived diffractograms from the lattice of AgCu NPs with 0%, 5%, 10%, and 15% Cu loading each exhibit spots that are consistent with scattering from an fcc lattice (Figure 2a and Figure S8). These data suggest that Cu incorporation does not appear to distort significantly the cubic Ag lattice and that the AgCu materials retain crystallographic order over the range of Cu loadings tested. Next, the elemental composition of the AgCu NPs was characterized by energy dispersive X-ray spectroscopy (EDS) to identify the actual Cu loading into the particles. EDS composition maps (Figure 2b and Figure S9) for AgCu NPs with 2.5%, 5%, and 7.5% nominal Cu loading clearly reflect the presence of both Ag and Cu in the particles. Analyses of EDS line scans acquired across AgCu NPs at the different Cu loadings (Figures S10 and S11) reveal a consistent spatial distribution of Ag and Cu up to 7.5% nominal loading. Average *d*-spacing values for the 0%, 2.5%, 5%, 7.5%, 10% and 15% AgCu NPs are comparable to the Ag(111) *d*-spacing value of 0.2325 nm (Figure 2c).[48] Collectively, these EDS and TEM data indicate the presence of small and uniformly distributed quantities of Cu in the Ag lattice at a level that avoids significant disruption of the lattice parameters. To perform a semiquantitative analysis of the Cu composition in the AgCu alloy NPs, we integrated the X-ray counts associated with the Lα = 0.93 keV, Kα = 8.04 keV, and Kβ = 8.91 keV[49] Cu lines (Figure 2d). These EDS analyses and elemental concentrations determined by inductively coupled plasma mass spectrometry provide evidence for a steady increase in % Cu content up to 7.5% nominal loading (Tables S2 and S3 and Figure S12). Therefore, we conclude that straightforward introduction of varying concentrations of Cu^{2+} during preparation of the metal-halide host is sufficient for tuning the percent Cu composition in the final AgCu NP.

Having established that our host−guest approach yields alloyed AgCu NPs whose composition can be tuned, we evaluated the activity and selectivity of these materials toward the electrocatalytic reduction of CO_2. The AgCu NPs were formulated as nanoparticle inks and then sprayed onto a gas diffusion layer to form a gas diffusion electrode (Figure S13). All data were collected under steady state conditions (Supporting Information, Materials and Methods). The faradaic efficiency (FE), which is a measure of the efficiency with which electrons participate in a given electrochemical transformation, was obtained for each of the AgCu NPs at 0%, 2.5%, 5%, 7.5%, 10%, and 15% nominal Cu loading at −0.5 V_{RHE} (Figure 3a). The major product from AgCu NP catalysis of the CO_2 reduction reaction (CO_2RR) was CO, and the product with the second highest yield was H_2. Only trace amounts of formate and acetate ($FE_{Formate}$ and $FE_{Acetate}$ at <1% of sampled product) were detected as liquid-phase products (Figure S14). Samples containing AgCu NPs with a 5% nominal Cu loading exhibited the highest FE_{CO}, namely, up to

https://doi.org/10.1021/acs.nanolett.4c02638
Nano Lett. 2024, 24, 13911−13918

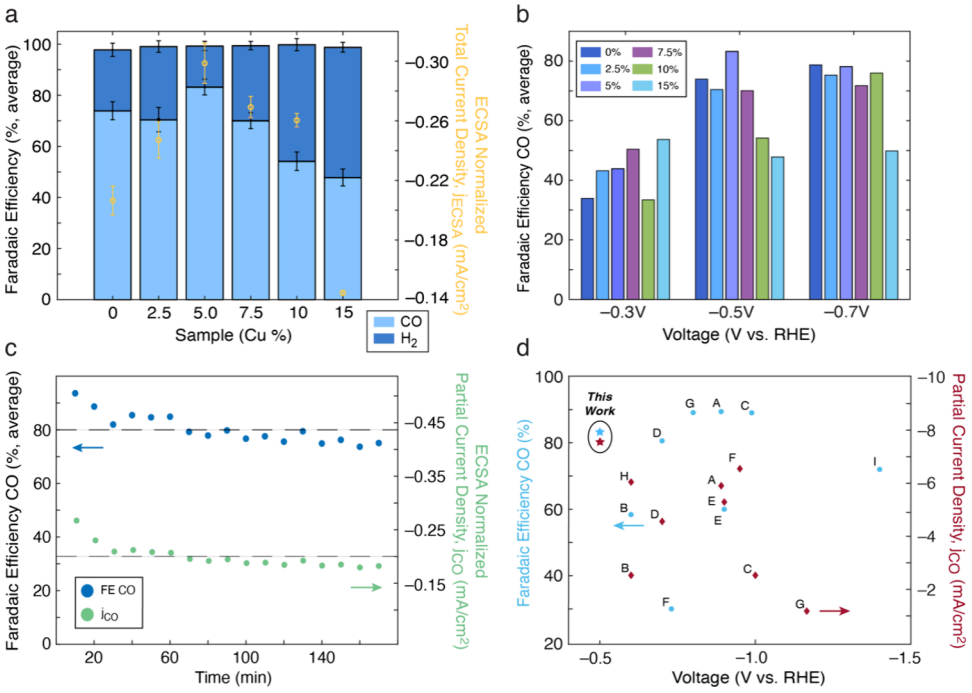

Figure 3. Data collected during the electrochemical CO_2 reduction reaction on a gas diffusion electrode loaded with AgCu NPs containing different Cu loadings. (a) Faradaic efficiencies of CO (FE_{CO}) and H_2 (FE_{H2}) product for samples with various % Cu loadings, at an overpotential of −0.5 V_{RHE}. The 5% Cu loading sample exhibits the highest FE_{CO} and highest suppression of H_2 products. An overlay of the ECSA normalized total current density plot (yellow markers) is also included. The current was normalized by the electrochemical active surface area of the sample (see Figure S15 and Table S4). Error bars represent the standard deviation of the data, with each data point representing an average of three trials. (b) FE_{CO} at −0.3 V_{RHE}, − 0.5 V_{RHE} and −0.7 V_{RHE} for all samples in the compositional range. The 5% Cu sample exhibits a maximum in catalytic selectivity. (c) Results from stability assessment of a 5% AgCu NP electrode performed over a 180 min period at −0.5 V_{RHE}. FE_{CO} and ECSA normalized partial current density j_{co} data were collected at 10 min intervals. (d) Comparison of the FE_{CO} and geometric partial current density j_{co} of this work (denoted by stars) to published Ag/Cu bimetallic material systems used as catalysts in the CO_2RR (A−I). Competitive selectivity and reaction efficiency are achieved by our nanoalloy at relatively mild overpotentials relative to prior work (Table S6).

85%. A 3-fold increase in targeted Cu loading (15%) resulted in a decrease in FE_{CO} to 50%. The specific activity of the AgCu NP electrodes was assessed by measuring the electrochemically active surface area (ECSA)-normalized (Figure S15 and Table S4) total current density, j_{ECSA}. Similar to the FE_{CO} trend, an increase in Cu loading from 0% to 5% resulted in an increase in j_{ECSA} from −0.2 mA/cm^2 to −0.3 mA/cm^2 at −0.5 V_{RHE}, with a significant decrease to −0.14 mA/cm^2 at 15% Cu loading.

To further assess the catalytic performance of the AgCu NP electrodes, the electrocatalyzed CO_2RR was performed on samples at each of the six Cu loading levels at overpotentials of −0.3, − 0.5, and −0.7 V_{RHE} (Figure 3b). At a relatively low overpotential of −0.3 V_{RHE}, all samples yield a lower FE_{CO} than at higher (more negative) overpotentials of −0.5 and −0.7 V_{RHE} (Figure S16). Hydrogen production from the catalysis of the competing hydrogen evolution reaction is more prevalent at the low overpotential of −0.3 V_{RHE} and from electrodes containing AgCu NPs with >10% Cu loading. At−0.5 V_{RHE}, a clear maximum in CO selectivity is seen for the 5% Cu electrode with an average FE_{CO} value of 83.23%. More negative overpotentials of −0.7 V_{RHE} yielded FE_{CO} values that stayed relatively constant for the 0% − 10% Cu electrodes, with a decrease to 50% FE at 15% Cu loading. We attribute the overall reduction in performance of the 15% Cu electrode to possible formation of Cu-rich phases (as the Cu solubility limit in Ag is exceeded, see Table S3) which exhibit high activity for hydrogen evolution reaction catalysis.

The use of bromide-containing precursors in the synthesis of metallic nanoparticles has been shown to yield products with chemisorbed Br^- present on some of their facets.[50] Some studies have indicated that the presence of halides on Cu surfaces can contribute to improving their catalytic selectivity.[51] To examine the extent of Br^- associated with our nanoparticle alloys, we investigated the composition of our NP alloy samples using X-ray photoelectron spectroscopy (XPS). An analysis of the ratio of Br 3d to Ag 3d peak areas for 2.5%, 5%, and 7.5% Cu alloy NPs after electrocatalysis indicates a consistently low ratio (<0.1) of Br to Ag for all three samples (Table S5). This reinforces the expectation that only *trace* amounts of Br^- are present in our samples. Moreover, Cu 2p XPS peaks collected at three independent regions across a 5% Cu NP alloy sample with *excess* bromide added (Supporting Information, Materials and Methods) appear at the same binding energy and have nearly identical intensities (Figure S17). Since the peak characteristics appear unaffected by the addition of Br^- to the catalyst ink, we conclude that bromide neither affects the electronic structure, nor the uniformity of Cu within the catalyst across large areas.

Finally, we assessed the influence of excess Br^- on the catalytic activity of our alloy NPs by comparing the catalytic performance of 5% AgCu NPs to 5% AgCu NPs with added LiBr. As confirmation that the LiBr addition did translate into increased loading of bromide that was retained by the NPs throughout the catalytic reaction, we observed an increased ratio of Br:Ag 3d peak areas for the 5% AgCu NP sample with

https://doi.org/10.1021/acs.nanolett.4c02638
Nano Lett. 2024, 24, 13911−13918

added LiBr after electrocatalysis (Table S5). Notably, the 5% AgCu NPs with excess bromide (through addition of 6 μL of 1 mol/L LiBr) exhibit a 42% decrease in the FE_{CO} and geometric j_{CO}, and a 3-fold increase in FE_{H2} and geometric j_{H2} for (Figure S18). These data indicate that *excess* Br^- negatively affects the catalytic selectivity and efficiency of the best performing 5% AgCu alloy NPs for CO product formation. We note that the amount of bromide added to the ink which resulted in this decrease in catalytic performance is much larger than the number of chemisorbed Br^- atoms we expect to be present on the surface of the AgCu alloys.[50] Collectively, the foregoing data and analyses suggest that residual Br^- intrinsically present within our catalytic formulation is unlikely to be significantly deteriorating the catalytic activity of our AgCu nanoalloys.

Based on measured FE_{CO}, j_{ECSA} and j_{CO} values, the 5% AgCu NP loaded electrode is the highest performing CO_2RR catalyst in our material series. The stability of the 5% AgCu NP was assessed by measuring the FE_{CO} and ECSA-normalized j_{CO} of the sample over a 180 min period at −0.5 V_{RHE} (Figure 3c and Figure S19). A 14% decrease in FE_{CO} across the 180 min sampling period, and a decrease in ECSA-normalized j_{CO} from −0.25 mA/cm^2 to −0.18 mA/cm^2, indicate that the NP catalysts did not undergo appreciable damage or decrease in activity during the stability measurements. Scanning electron microscopy (SEM) imaging of the electrodes before and after the 180 min stability assessment revealed no apparent surface reconstruction or visible material loss (Figure S20).

The activity and selectivity of the AgCu NPs synthesized in this work were compared to various literature examples of Ag/Cu bimetallic materials used as catalysts for the CO_2RR (Figure 3d). With an FE of 83.23% and j_{CO} of 7.52 mA/cm^2, our 5% Cu in Ag nanoalloy is, at much less negative overpotentials, comparably selective to and more than three times more active than Cu@Ag core−shell nanoparticles (ref C in Figure 3d and Table S6), and also performs well compared to other Ag/Cu containing nanostructures. Moreover, our material yields these values at modest overpotentials and at mass loadings of 0.2 mg/cm^2, which are approximately 2 to 5 times lower than a majority of the highlighted examples. Such high mass efficiency is a notable feature of our nanocatalyst. Our AgCu nanoalloy catalyst platform also offers structural advantages. High material porosity, such as that exhibited by the bimetallic foams,[34,52] aerogels,[35] and sponge-like[53] systems included in our comparison, is closely associated with catalytic activity. When deposited on the electrode surface, our AgCu NPs form a highly active, porous network, and also appear to retain their individual structural and electronic integrity during electrocatalysis (Figures S20−S22). Compared to large-network foam or gel systems our precisely tunable and structurally robust AgCu NPs more readily serve as effective platforms for probing structure-catalytic property relationships and determining the source of their increased performance.

To better understand the mechanism of CO_2 reduction on our AgCu NPs, we performed CO_2RR experiments across a range of temperatures at a fixed potential of −0.5 V_{RHE} (Figure 4). As temperature was increased from 25 °C to 40 °C a systematic increase in FE_{CO} was observed for each AgCu NP sample (Figure S23). These CO_2RR experiments were used to furnish an Arrhenius plot of partial current density of CO (j_{CO}) as a function of the inverse of absolute temperature for each of the 0−15% AgCu NP samples. The activation energy for the formation of CO (extracted from the slope of the Arrhenius plot) initially decreases as a function of increasing Cu loading, with the 5% AgCu NP samples exhibiting the lowest E_a of 19.01 kJ/mol. As Cu loading increases beyond 5%, there is a monotonic increase in the activation energy to 37.69 kJ/mol. This trend indicates that CO production is highly sensitive to the amount of Cu loading within the AgCu nanoalloys and that the 5% AgCu NP sample presents the lowest energy barrier for CO formation. Moreover, this coincides with the trend of CO activity (j_{CO}) for all AgCu particles. It is likely that the lower activation energy for CO formation exhibited by the 5% AgCu NP sample stems from a lower adsorption barrier of the CO intermediate due to electronic effects between Ag and Cu, which are intimately coupled at the solubility limit of this nanoalloy.[54]

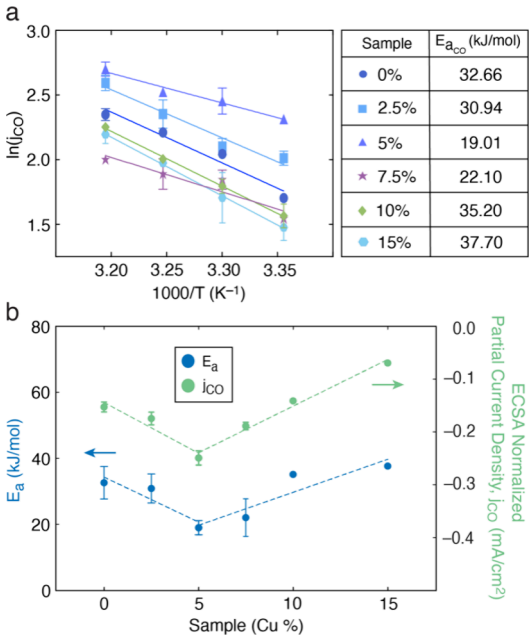

Figure 4. (a) Arrhenius plot of temperature dependent activity of the 0−15% AgCu NP catalysts as CO_2 reduction is performed (at −0.5 V_{RHE} in 1 mol/L KOH) on a gas diffusion electrode. Table: summary of E_a values (kJ/mol) calculated from the slope of each sample line. (b) Overlay of the activation energy for CO production and ECSA normalized partial current density j_{CO} for the 0−15% AgCu NP samples. Error bars represent the standard deviation of the data, with each data point representing an average of three trials.

We have presented a versatile host−guest synthetic platform to prepare compositionally tuned alloy nanoparticles and have identified an optimized AgCu electrocatalyst for CO_2 reduction.

■ ASSOCIATED CONTENT

Supporting Information

The Supporting Information is available free of charge at https://pubs.acs.org/doi/10.1021/acs.nanolett.4c02638.

Detailed nanoparticle catalyst synthesis protocols, sample preparation and characterization, electrocatalysis protocols, electrochemical analyses, size distributions of nanoparticles at key stages of synthesis, UV−vis spectra of nanoparticles at key stages of synthesis, TEM images and associated diffractograms, EDS maps and line scans, ICPMS data, electrochemical data and analyses (e.g., cyclic voltammograms, UPD analyses, results of CO_2RR at various temperatures), NMR of liquid products,

https://doi.org/10.1021/acs.nanolett.4c02638
Nano Lett. 2024, 24, 13911−13918

description of quantification of gas products via gas diffusion electrode, SEM images and atom-resolution HAADF images and EDS maps of AgCu NPs before and after electrocatalysis, and quantitative data tables (e.g, mass loadings, EDS data, ICPMS analyses, ECSA analysis, literature comparisons, and electrode calibration data) (PDF)

AUTHOR INFORMATION

Corresponding Authors

Anthony Shoji Hall − *Department of Materials Science and Engineering, Johns Hopkins University, Baltimore, Maryland 21218, United States of America;* orcid.org/0000-0003-4134-4160; Email: shoji@jhu.edu

Thomas J. Kempa − *Department of Chemistry and Department of Materials Science and Engineering, Johns Hopkins University, Baltimore, Maryland 21218, United States of America;* orcid.org/0000-0002-1672-8325; Email: tkempa@jhu.edu

Authors

Marta Śliwa − *Department of Chemistry, Johns Hopkins University, Baltimore, Maryland 21218, United States of America*

Hao Zhang − *Department of Materials Science and Engineering, Johns Hopkins University, Baltimore, Maryland 21218, United States of America*

Jiaxin Gao − *Department of Materials Science and Engineering, Johns Hopkins University, Baltimore, Maryland 21218, United States of America*

Benjamin O. Stephens − *Department of Chemistry, Johns Hopkins University, Baltimore, Maryland 21218, United States of America*

Andrew J. Patera − *Department of Chemistry, Johns Hopkins University, Baltimore, Maryland 21218, United States of America*

David Raciti − *Materials Science and Engineering Division, National Institute of Standards and Technology, Gaithersburg, Maryland 20899, United States of America;* orcid.org/0000-0002-9580-4524

Paul D. Hanrahan − *Department of Chemistry, Johns Hopkins University, Baltimore, Maryland 21218, United States of America*

Zoey A. Warecki − *Materials Science and Technology Division, U.S. Naval Research Laboratory, Washington D.C. 20375, United States of America*

Daniel L. Foley − *Department of Materials Science and Engineering, Johns Hopkins University, Baltimore, Maryland 21218, United States of America*

Kenneth JT Livi − *Department of Materials Science and Engineering, Johns Hopkins University, Baltimore, Maryland 21218, United States of America;* orcid.org/0000-0001-7728-5460

Todd H. Brintlinger − *Materials Science and Technology Division, U.S. Naval Research Laboratory, Washington D.C. 20375, United States of America*

Mitra L. Taheri − *Department of Materials Science and Engineering, Johns Hopkins University, Baltimore, Maryland 21218, United States of America;* orcid.org/0000-0001-5349-1411

Complete contact information is available at: https://pubs.acs.org/10.1021/acs.nanolett.4c02638

Author Contributions

M.S. and H.Z. contributed equally to this work. M.S., A.S.H., and T.J.K. designed the study. M.S. and H.Z. performed all experiments with input from T.J.K. and A.S.H. All authors contributed to data analyses. The manuscript was written with contributions from all authors. All authors have approved the final version of the manuscript.

Funding

T.J.K. acknowledges funding from a National Science Foundation (DMR-1848046) CAREER grant which supported characterization studies in this work. A.S.H. acknowledges funding from a National Science Foundation (CHE-2102648) grant and a National Science Foundation (CBET-2326720) grant which supported this work. T.H.B. and Z.A.W. gratefully acknowledge the Office of Naval Research for financial support through the NRL base program.

Notes

The authors declare no competing financial interest.

ABBREVIATIONS

CO_2RR: carbon-dioxide reduction reaction
FE: Faradaic efficiency
TEM: transmission electron microscopy
HAADF: high-angle annular dark field
BF: bright-field
UV−vis: UV−visible spectroscopy
EDS: energy dispersive X-ray spectroscopy
FFT: fast-Fourier transform
SEM: scanning electron microscopy
UPD: underpotential deposition
XPS: X-ray photoelectron spectroscopy

REFERENCES

(1) Chiang, I.-C.; Chen, D.-H. Synthesis of Monodisperse FeAu Nanoparticles with Tunable Magnetic and Optical Properties. *Adv. Funct. Mater.* **2007**, *17* (8), 1311−1316.

(2) Scarabelli, L.; Coronado-Puchau, M.; Giner-Casares, J. J.; Langer, J.; Liz-Marzán, L. M. Monodisperse Gold Nanotriangles: Size Control, Large-Scale Self-Assembly, and Performance in Surface-Enhanced Raman Scattering. *ACS Nano* **2014**, *8* (6), 5833−5842.

(3) Juodėnas, M.; Tamulevičius, T.; Henzie, J.; Erts, D.; Tamulevičius, S. Surface Lattice Resonances in Self-Assembled Arrays of Monodisperse Ag Cuboctahedra. *ACS Nano* **2019**, *13* (8), 9038−9047.

(4) Xing, L.; Xiahou, Y.; Zhang, P.; Du, W.; Xia, H. Size Control Synthesis of Monodisperse, Quasi-Spherical Silver Nanoparticles To Realize Surface-Enhanced Raman Scattering Uniformity and Reproducibility. *ACS Appl. Mater. Interfaces* **2019**, *11* (19), 17637−17646.

(5) Grancharov, S. G.; Zeng, H.; Sun, S.; Wang, S. X.; O'Brien, S.; Murray, C. B.; Kirtley, J. R.; Held, G. A. Bio-Functionalization of Monodisperse Magnetic Nanoparticles and Their Use as Biomolecular Labels in a Magnetic Tunnel Junction Based Sensor. *J. Phys. Chem. B* **2005**, *109* (26), 13030−13035.

(6) Tang, L.; Fan, T. M.; Borst, L. B.; Cheng, J. Synthesis and Biological Response of Size-Specific, Monodisperse Drug−Silica Nanoconjugates. *ACS Nano* **2012**, *6* (5), 3954−3966.

(7) Shen, L.; Bao, J.; Wang, D.; Wang, Y.; Chen, Z.; Ren, L.; Zhou, X.; Ke, X.; Chen, M.; Yang, A. One-Step Synthesis of Monodisperse, Water-Soluble Ultra-Small Fe3O4 Nanoparticles for Potential Bio-Application. *Nanoscale* **2013**, *5* (5), 2133−2141.

(8) Si, P.; Yuan, E.; Liba, O.; Winetraub, Y.; Yousefi, S.; SoRelle, E. D.; Yecies, D. W.; Dutta, R.; de la Zerda, A. Gold Nanoprisms as Optical Coherence Tomography Contrast Agents in the Second Near-

Infrared Window for Enhanced Angiography in Live Animals. *ACS Nano* **2018**, *12* (12), 11986−11994.
(9) Park, G.; Seo, D.; Jung, J.; Ryu, S.; Song, H. Shape Evolution and Gram-Scale Synthesis of Gold@Silver Core−Shell Nanopolyhedrons. *J. Phys. Chem. C* **2011**, *115* (19), 9417−9423.
(10) Jukk, K.; Kongi, N.; Tammeveski, K.; Solla-Gullón, J.; Feliu, J. M. PdPt Alloy Nanocubes as Electrocatalysts for Oxygen Reduction Reaction in Acid Media. *Electrochem. Commun.* **2015**, *56*, 11−15.
(11) Gao, C.; Hu, Y.; Wang, M.; Chi, M.; Yin, Y. Fully Alloyed Ag/Au Nanospheres: Combining the Plasmonic Property of Ag with the Stability of Au. *J. Am. Chem. Soc.* **2014**, *136* (20), 7474−7479.
(12) Chen, J.; Feng, J.; Yang, F.; Aleisa, R.; Zhang, Q.; Yin, Y. Space-Confined Seeded Growth of Cu Nanorods with Strong Surface Plasmon Resonance for Photothermal Actuation. *Angew. Chem.* **2019**, *131* (27), 9376−9382.
(13) Srinoi, P.; Chen, Y.-T.; Vittur, V.; Marquez, M. D.; Lee, T. R. Bimetallic Nanoparticles: Enhanced Magnetic and Optical Properties for Emerging Biological Applications. *Applied Sciences* **2018**, *8* (7), 1106.
(14) García-Diéguez, M.; Finocchio, E.; Larrubia, M. Á.; Alemany, L. J.; Busca, G. Characterization of Alumina-Supported Pt, Ni and PtNi Alloy Catalysts for the Dry Reforming of Methane. *J. Catal.* **2010**, *274* (1), 11−20.
(15) Lin, M.-L.; Lo, M.-Y.; Mou, C.-Y. PtRuP Nanoparticles Supported on Mesoporous Carbon Thin Film as Highly Active Anode Materials for Direct Methanol Fuel Cell. *Catal. Today* **2011**, *160* (1), 109−115.
(16) Hou, S.; Xu, Y.; Liu, Y.; Xu, R.; Zhang, B. Room-Temperature Fast Synthesis of Composition-Adjustable Pt−Pd Alloy Sub-10-Nm Nanoparticle Networks with Improved Electrocatalytic Activities. *Chem. Lett.* **2012**, *41* (5), 546−548.
(17) Liu, J.-H.; Wang, A.-Q.; Chi, Y.-S.; Lin, H.-P.; Mou, C.-Y. Synergistic Effect in an Au−Ag Alloy Nanocatalyst: CO Oxidation. *J. Phys. Chem. B* **2005**, *109* (1), 40−43.
(18) Luo, J.; Njoki, P. N.; Lin, Y.; Wang, L.; Zhong, C. J. Activity-Composition Correlation of AuPt Alloy Nanoparticle Catalysts in Electrocatalytic Reduction of Oxygen. *Electrochem. Commun.* **2006**, *8* (4), 581−587.
(19) Cai, S.; Qi, C.; Li, Y.; Han, Q.; Yang, R.; Wang, C. PtCo Bimetallic Nanoparticles with High Oxidase-like Catalytic Activity and Their Applications for Magnetic-Enhanced Colorimetric Biosensing. *J. Mater. Chem. B* **2016**, *4* (10), 1869−1877.
(20) Li, H.; Wu, H.; Zhai, Y.; Xu, X.; Jin, Y. Synthesis of Monodisperse Plasmonic Au Core−Pt Shell Concave Nanocubes with Superior Catalytic and Electrocatalytic Activity. *ACS Catal.* **2013**, *3* (9), 2045−2051.
(21) Sun, X.; Yang, Y.; Zhang, Z.; Qin, D. Mechanistic Roles of Hydroxide in Controlling the Deposition of Gold on Colloidal Silver Nanocrystals. *Chem. Mater.* **2017**, *29* (9), 4014−4021.
(22) Akiyoshi, K.; Watanabe, Y.; Kameyama, T.; Kawawaki, T.; Negishi, Y.; Kuwabata, S.; Torimoto, T. Composition Control of Alloy Nanoparticles Consisting of Bulk-Immiscible Au and Rh Metals via an Ionic Liquid/Metal Sputtering Technique for Improving Their Electrocatalytic Activity. *Phys. Chem. Chem. Phys.* **2022**, *24* (39), 24335−24344.
(23) Vasquez, Y.; Luo, Z.; Schaak, R. E. Low-Temperature Solution Synthesis of the Non-Equilibrium Ordered Intermetallic Compounds Au3Fe, Au3Co, and Au3Ni as Nanocrystals. *J. Am. Chem. Soc.* **2008**, *130* (36), 11866−11867.
(24) Thota, S.; Wang, Y.; Zhao, J. Colloidal Au−Cu Alloy Nanoparticles: Synthesis, Optical Properties and Applications. *Mater. Chem. Front.* **2018**, *2* (6), 1074−1089.
(25) Amendola, V.; Meneghetti, M.; Bakr, O. M.; Riello, P.; Polizzi, S.; Anjum, D. H.; Fiameni, S.; Arosio, P.; Orlando, T.; Fernandez, C. de J.; Pineider, F.; Sangregorio, C.; Lascialfari, A. Coexistence of Plasmonic and Magnetic Properties in Au89Fe11 Nanoalloys. *Nanoscale* **2013**, *5* (12), 5611−5619.
(26) Hoang, T. T. H.; Verma, S.; Ma, S.; Fister, T. T.; Timoshenko, J.; Frenkel, A. I.; Kenis, P. J. A.; Gewirth, A. A. Nanoporous Copper−Silver Alloys by Additive-Controlled Electrodeposition for the Selective Electroreduction of CO2 to Ethylene and Ethanol. *J. Am. Chem. Soc.* **2018**, *140* (17), 5791−5797.
(27) Peterson, A. A.; Abild-Pedersen, F.; Studt, F.; Rossmeisl, J.; Nørskov, J. K. How Copper Catalyzes the Electroreduction of Carbon Dioxide into Hydrocarbon Fuels. *Energy Environ. Sci.* **2010**, *3* (9), 1311−1315.
(28) Nie, X.; Esopi, M. R.; Janik, M. J.; Asthagiri, A. Selectivity of CO2 Reduction on Copper Electrodes: The Role of the Kinetics of Elementary Steps. *Angew. Chem.* **2013**, *125* (9), 2519−2522.
(29) Rice, K. P.; Walker, E. J., Jr.; Stoykovich, M. P.; Saunders, A. E. Solvent-Dependent Surface Plasmon Response and Oxidation of Copper Nanocrystals. *J. Phys. Chem. C* **2011**, *115* (5), 1793−1799.
(30) Chan, G. H.; Zhao, J.; Hicks, E. M.; Schatz, G. C.; Van Duyne, R. P. Plasmonic Properties of Copper Nanoparticles Fabricated by Nanosphere Lithography. *Nano Lett.* **2007**, *7* (7), 1947−1952.
(31) *Desk Handbook: Phase Diagrams for Binary Alloys*, 2nd ed.; Okamoto, H., Ed.; ASM International: 2010.
(32) Miyajima, K.; Fukushima, N.; Himeno, H.; Yamada, A.; Mafuné, F. Breakdown of the Hume−Rothery Rules in Sub-Nanometer-Sized Ta-Containing Bimetallic Small Clusters. *J. Phys. Chem. A* **2009**, *113* (48), 13448−13450.
(33) Miyajima, K.; Himeno, H.; Yamada, A.; Yamamoto, H.; Mafuné, F. Nanoalloy Formation of Ta-Containing Trimetallic Small Clusters. *J. Phys. Chem. A* **2011**, *115* (9), 1516−1520.
(34) Kottakkat, T.; Klingan, K.; Jiang, S.; Jovanov, Z. P.; Davies, V. H.; El-Nagar, G. A. M.; Dau, H.; Roth, C. Electrodeposited AgCu Foam Catalysts for Enhanced Reduction of CO2 to CO. *ACS Appl. Mater. Interfaces* **2019**, *11* (16), 14734−14744.
(35) Wang, W.; Gong, S.; Liu, J.; Ge, Y.; Wang, J.; Lv, X. Ag-Cu Aerogel for Electrochemical CO2 Conversion to CO. *J. Colloid Interface Sci.* **2021**, *595*, 159−167.
(36) Huang, J.; Mensi, M.; Oveisi, E.; Mantella, V.; Buonsanti, R. Structural Sensitivities in Bimetallic Catalysts for Electrochemical CO2 Reduction Revealed by Ag−Cu Nanodimers. *J. Am. Chem. Soc.* **2019**, *141* (6), 2490−2499.
(37) Freire, R. M.; Rojas-Nunez, J.; Elias-Arriaga, A. L.; Fujisawa, K.; Troncoso, L.; Denardin, J. C.; Baltazar, S. E. Natural Arrangement of AgCu Bimetallic Nanostructures through Oleylamine Reduction. *Inorg. Chem. Front.* **2020**, *7* (24), 4902−4912.
(38) Chang, Z.; Huo, S.; Zhang, W.; Fang, J.; Wang, H. The Tunable and Highly Selective Reduction Products on Ag@Cu Bimetallic Catalysts Toward CO2 Electrochemical Reduction Reaction. *J. Phys. Chem. C* **2017**, *121* (21), 11368−11379.
(39) Rahman, L.; Qureshi, R.; Yasinzai, M. M.; Shah, A. Synthesis and Spectroscopic Characterization of Ag-Cu Alloy Nanoparticles Prepared in Various Ratios. *Comptes Rendus Chimie* **2012**, *15* (6), 533−538.
(40) Dou, Q.; Li, Y.; Wong, K. W.; Ng, K. M. Facile Synthesis of Nearly Monodisperse AgCu Alloy Nanoparticles with Synergistic Effect against Oxidation and Electromigration. *J. Mater. Res.* **2019**, *34* (12), 2095−2104.
(41) Yang, C.; Ko, B. H.; Hwang, S.; Liu, Z.; Yao, Y.; Luc, W.; Cui, M.; Malkani, A. S.; Li, T.; Wang, X.; Dai, J.; Xu, B.; Wang, G.; Su, D.; Jiao, F.; Hu, L. Overcoming Immiscibility toward Bimetallic Catalyst Library. *Science Advances* **2020**, *6* (17), No. eaaz6844.
(42) Kossak, A. E.; Stephens, B. O.; Tian, Y.; Liu, P.; Chen, M.; Kempa, T. J. Anisotropic and Multicomponent Nanostructures by Controlled Symmetry Breaking of Metal Halide Intermediates. *Nano Lett.* **2018**, *18* (4), 2324−2328.
(43) Halas, N. J.; Lal, S.; Chang, W.-S.; Link, S.; Nordlander, P. Plasmons in Strongly Coupled Metallic Nanostructures. *Chem. Rev.* **2011**, *111* (6), 3913−3961.
(44) Lee, J.; Hasan, W.; Stender, C. L.; Odom, T. W. Pyramids: A Platform for Designing Multifunctional Plasmonic Particles. *Acc. Chem. Res.* **2008**, *41* (12), 1762−1771.
(45) Chowdhury, S.; Bhethanabotla, V. R.; Sen, R. Effect of Ag−Cu Alloy Nanoparticle Composition on Luminescence Enhancement/Quenching. *J. Phys. Chem. C* **2009**, *113* (30), 13016−13022.

https://doi.org/10.1021/acs.nanolett.4c02638
Nano Lett. 2024, 24, 13911−13918

(46) Zhou, M.; Wang, Z.; Sun, Q.; Wang, J.; Zhang, C.; Chen, D.; Li, X. High-Performance Ag−Cu Nanoalloy Catalyst for the Selective Catalytic Oxidation of Ammonia. *ACS Appl. Mater. Interfaces* **2019**, *11* (50), 46875−46885.
(47) Rahman, L.; Shah, A.; Lunsford, S. K.; Han, C.; Nadagouda, M. N.; Sahle-Demessie, E.; Qureshi, R.; Khan, M. S.; Kraatz, H.-B.; Dionysiou, D. D. Monitoring of 2-Butanone Using a Ag−Cu Bimetallic Alloy Nanoscale Electrochemical Sensor. *RSC Adv.* **2015**, *5* (55), 44427−44434.
(48) Chen, R.; Nuhfer, N. T.; Moussa, L.; Morris, H. R.; Whitmore, P. M. Silver Sulfide Nanoparticle Assembly Obtained by Reacting an Assembled Silver Nanoparticle Template with Hydrogen Sulfide Gas. *Nanotechnology* **2008**, *19* (45), 455604.
(49) Krause, M. O.; Oliver, J. H. Natural Widths of Atomic K and L Levels, Kα X-ray Lines and Several KLL Auger Lines. *J. Phys. Chem. Ref. Data* **1979**, *8* (2), 329−338.
(50) Peng, H.-C.; Xie, S.; Park, J.; Xia, X.; Xia, Y. Quantitative Analysis of the Coverage Density of Br− Ions on Pd{100} Facets and Its Role in Controlling the Shape of Pd Nanocrystals. *J. Am. Chem. Soc.* **2013**, *135* (10), 3780−3783.
(51) Yuan, X.; Lee, K.; Schmidt, J. R.; Choi, K.-S. Halide Adsorption Enhances Electrochemical Hydrogenolysis of 5-Hydroxymethylfurfural by Suppressing Hydrogenation. *J. Am. Chem. Soc.* **2023**, *145* (37), 20473−20484.
(52) Lee, H.; Kim, S.-K.; Ahn, S. H. Electrochemical Preparation of Ag/Cu and Au/Cu Foams for Electrochemical Conversion of CO2 to CO. *Journal of Industrial and Engineering Chemistry* **2017**, *54*, 218−225.
(53) Zhang, W.; Xu, C.; Hu, Y.; Yang, S.; Ma, L.; Wang, L.; Zhao, P.; Wang, C.; Ma, J.; Jin, Z. Electronic and Geometric Structure Engineering of Bicontinuous Porous Ag−Cu Nanoarchitectures for Realizing Selectivity-Tunable Electrochemical CO2 Reduction. *Nano Energy* **2020**, *73*, No. 104796.
(54) Clark, E. L.; Hahn, C.; Jaramillo, T. F.; Bell, A. T. Electrochemical CO2 Reduction over Compressively Strained CuAg Surface Alloys with Enhanced Multi-Carbon Oxygenate Selectivity. *J. Am. Chem. Soc.* **2017**, *139* (44), 15848−15857.

https://doi.org/10.1021/acs.nanolett.4c02638
Nano Lett. 2024, 24, 13911−13918